



# Membraneless unbuffered seawater electrolysis for pure hydrogen production using PtRuTiO<sub>x</sub> anode and MnO<sub>x</sub> cathode pairs

Nan-Nan Liang<sup>a</sup>, Dong Suk Han<sup>b</sup>, Hyunwoong Park<sup>a,\*</sup>

<sup>a</sup> School of Energy Engineering, Kyungpook National University, Daegu 41566, Republic of Korea

<sup>b</sup> Center for Advanced Materials, Qatar University, Doha 2713, Qatar

## ARTICLE INFO

### Keywords:

Electrocatalyst

Selectivity

Chloride oxidation reaction

Oxygen evolution reaction

Hydrogen production reaction

## ABSTRACT

Seawater electrolysis is promising as an in situ H<sub>2</sub> production method, allowing immediate overseas transport of the produced H<sub>2</sub>. In this study, membraneless electrolysis of undisturbed, unbuffered seawater (pH 8.2) is proposed to produce high-purity H<sub>2</sub>. A ternary Pt, Ru, and Ti (PRT) catalyst with a minimized Pt level (Pt<sub>0.06</sub>Ru<sub>0.24</sub>Ti<sub>0.70</sub>O<sub>x</sub>) drives chloride oxidation reaction (ClOR) at a Faradaic efficiency (FE) of ~100% in saline water at current density (*J*) of 800 mA cm<sup>-2</sup> over 500 h. Chlorine reduction reaction (ClRR) is also inhibited on MnO<sub>x</sub> electrodes, leading to hydrogen evolution reaction (HER) at an FE of ~100% even in the presence of chlorine species (HClO/ClO<sup>-</sup>). Finally, the PRT anode/MnO<sub>x</sub> cathode pair is demonstrated to drive ClOR and HER at FEs of ~100% at *J* = 80 mA cm<sup>-2</sup> over 100 h in a single-compartment cell containing seawater. Oxygen evolution reaction and ClRR are completely inhibited during seawater electrolysis.

## 1. Introduction

Electrolytic hydrogen production is considered a key energy transition, carbon-neutral technology when coupled with renewable energy production processes [1–9]. The minimum H<sub>2</sub> production cost was estimated to decrease from \$4.56 kg<sup>-1</sup> in 2020 to \$2.44 kg<sup>-1</sup> in 2050 upon direct connection with solar- and wind-powered grids [10,11]. As the H<sub>2</sub> price is highly dependent on geographic location, the maritime transport of as-produced H<sub>2</sub> at low costs to locations where the H<sub>2</sub> production is unfavorable is an alternative. In this regard, seawater electrolysis is promising for in situ H<sub>2</sub> production and overseas transport. Harvesting renewable energy and directly connecting it to the electrolyzer further increases the technical readiness of seawater electrolysis [4,12,13].

Although the conventional electrolysis has been extensively studied in well-defined aqueous environment characteristics (e.g., electrolyte and pH), such conditions cannot be directly applied to the seawater electrolysis at a pH ~8.2 because of the presence of several types of natural inorganic species [6,14–17]. Among them, chlorides seriously interfere with oxygen and hydrogen evolution reactions (OER and HER, respectively) [7,18,19]. The electrochemical potentials of chloride oxidation reaction (ClOR, reaction 1 at *E*<sup>0</sup> = 1.482 V) and OER (*E*<sup>0</sup> = 1.229 V) are similar, but the ClOR with two-electron transfer becomes

dominant [20–24], particularly at high current densities.



In addition, the chlorine reduction reaction (ClRR, a reverse of ClOR) with the as-produced chlorines (represented by the HClO/ClO<sup>-</sup> pair, *pK*<sub>a</sub> = 7.46) competes with HER [8,9,19,22,23,25]. The active involvement of ClOR/ClRR eventually reduces the Faradaic efficiencies (FEs) of O<sub>2</sub> and H<sub>2</sub> production.

To address this challenge, a membraned alkaline electrolysis system has often been employed for seawater electrolysis [14,26,27]. An increase in the pH of seawater reduces both *E*<sup>0</sup><sub>OER</sub> and *E*<sup>0</sup><sub>ClOR</sub> to different degrees (e.g., *E*<sup>0</sup><sub>OER</sub> = 0.401 V and *E*<sup>0</sup><sub>ClOR</sub> = 0.81 at pH 14), and the OER becomes dominant over the ClOR [26,28]. Even if ClOR occurs concurrently, the employed membranes separate evolved O<sub>2</sub> and H<sub>2</sub> gases as well as inhibit the crossover of HClO to the catholyte. Accordingly, the negative effects of ClOR/ClRR are minimized. Although feasible, however, the synthesis of OER-selective catalyst durably working at a large *J* in seawater is difficult. In addition, the use of membranes and corrosive KOH significantly increases the H<sub>2</sub> production cost [29,30]. Furthermore, dissolved organic substances (~90% of the total organic carbon in the oceans) interfere with the OER and cause fouling of the membranes [31,32].

With this in mind, we propose a membraneless electrolysis of

\* Corresponding author.

E-mail address: [hwp@knu.ac.kr](mailto:hwp@knu.ac.kr) (H. Park).

<https://doi.org/10.1016/j.apcatb.2022.122275>

Received 20 June 2022; Received in revised form 24 November 2022; Accepted 6 December 2022

Available online 9 December 2022

0926-3373/© 2022 Elsevier B.V. All rights reserved.

unperturbed, unbuffered seawater at pH 8.2 for the production of high-purity  $H_2$ . To achieve this goal, we attempted to synthesize ClOR-selective anodes and ClRR-inhibitive cathodes, while completely retarding the OER at the anode and maximizing the HER at the cathode (Scheme 1). If the ClOR and HER are coupled, high-purity  $H_2$  gas without  $O_2$  can be obtained with no need of a membrane because the as-formed chlorines remain in the aqueous phase. For selective ClOR, dimensionally stable anodes (DSAs) primarily composed of  $IrO_2$  are typically used [33]. However, their high synthetic cost limits their practical applicability. To reduce the cost, a fraction of the expensive Ir is often replaced with relatively inexpensive metals (e.g., Ru), and the IrRu catalyst is mixed with support oxides (e.g.,  $TiO_2$  and  $SnO_2$ ) [7,16,34,35]. Unfortunately, the modified electrodes exhibit reduced activity for ClOR, particularly under mild chloride concentrations. Recently, atomically dispersed Pt on carbon nanotubes was reported to be catalytically active for ClOR in 0.1 M NaCl [36]. This suggests that in addition to Ru, Pt can be active toward ClOR and replace the approximately five-fold expensive Ir, but only if discrete Pt and Ru nanoparticles are well dispersed on the support oxides. Meanwhile, Cr(VI) ions are conventionally used in undivided electrolyzers to inhibit ClRR and selectively drive the HER. The added Cr(VI) ions form a thin (hydr)oxide film on the cathode during electrolysis, thereby blocking chlorine access [37]. Instead of adding toxic Cr(VI) ions, the cathode surface can be passivated with (hydr)oxides prior to electrolysis [38]. For example,  $MnO_x$  can effectively inhibit ClRR and drive the HER at an FE of  $\sim 95\%$  [25]. Although promising, the cathodic reactions with  $MnO_x$  were not coupled to the anodic reactions (ClOR and OER). This suggests that the effect of  $MnO_x$  in a full reaction needs to be further studied and confirmed. In this study, we synthesized ternary Pt, Ru, and Ti oxide (PRT) anodes and  $MnO_x$  cathodes for selective ClOR and HER, respectively. An optimized PRT electrocatalyst with a minimized Pt level ( $Pt_{0.06}Ru_{0.24}Ti_{0.7}O_x$ ) drove ClOR at an FE of  $\sim 100\%$  in saline water at an

industrial level of  $J$  ( $0.8\text{ A cm}^{-2}$ ) over 500 h. Furthermore, ClRR was effectively inhibited by the  $MnO_x$  cathode, leading to  $\sim 100\%$  FE in the  $H_2$  production. Finally, the PRT anode and  $MnO_x$  cathode pair produced aqueous free chlorine and  $H_2$  gas with FEs of  $\sim 100\%$  over 100 h in a single-compartment cell containing seawater at pH 8.2.

## 2. Experimental

### 2.1. Synthesis and surface characterization of materials

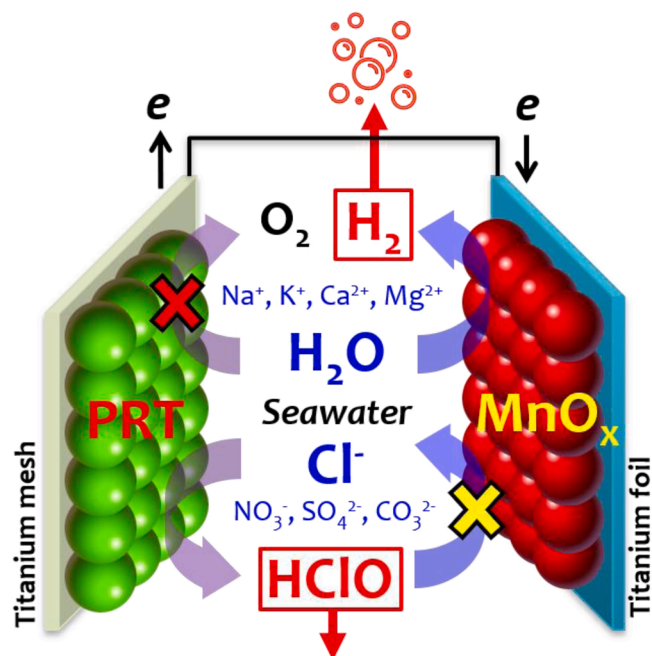
Analytical grade chemical reagents and solvents were purchased from Sigma-Aldrich and used without further purification, unless otherwise mentioned. Titanium meshes ( $1\text{ cm} \times 3\text{ cm}$ , 1-mm thick, Alfa Aesar) and foils (0.127-mm thick, 99.7% pure, Aldrich) were rubbed with sand paper, washed with deionized water ( $18\text{ M}\Omega\text{ cm}$ ) and ethanol, and subsequently treated with aqueous HCl (37%) solution for 20 min at  $50^\circ\text{C}$ . In sequence, the substrates were washed with excess deionized water and ethanol. For the synthesis of ternary ( $Pt_{0.2}Ru_{0.8}$ ) $_xTi_{1-x}O_y$  (PRT- $x$ ) particles ( $x = 0.1\text{--}0.4$ ), various ratios of  $H_2PtCl_6 \cdot H_2O$  (dissolved in 0.1 mL HCl),  $RuCl_3 \cdot H_2O$  (dissolved in 0.1 mL HCl), and  $Ti(C_4H_9O)_4$  (dissolved in 0.5 mL ethanol) were mixed in a mixed solution of citric acid ( $C_6H_8O_7$ , Duksan, 99.5%) and ethylene glycol ( $C_2H_6O_2$ , Daejung, 99.5%) (1/4 by molar ratio) at  $90^\circ\text{C}$ . After mixing for 5 min, the PRT samples were annealed at various temperatures ( $400\text{--}900^\circ\text{C}$ ) for 1 h in air. The as-obtained PRT powder (10 mg) was dispersed in 2-propanol (2 mL,  $C_3H_8O$ , Duksan, 99.9%) using ultrasound for 2 h. This PRT slurry was sprayed onto Ti meshes with an air gun at loading masses of  $0.83\text{--}3.33\text{ mg cm}^{-2}$ . Subsequently, the PRT/Ti samples were dried overnight in air. Unless otherwise specified, PRT represents the sample for  $x = 0.3$  (i.e.,  $Pt_{0.06}Ru_{0.24}Ti_{0.7}O_y$ ) annealed at  $500^\circ\text{C}$  with a loading mass of  $3.33\text{ mg cm}^{-2}$ . For comparison, binary  $Pt_{0.2}Ru_{0.8}O_y$  (PR, i.e., PRT with  $x = 1$ ) was synthesized at  $500^\circ\text{C}$  for 1 h in air.

For the  $MnO_x$  electrodes, a  $Mn(NO_3)_2$  ( $>97\%$ ) solution (2 M, dissolved in 10  $\mu\text{L}$  ethanol) was evenly dispersed over the Ti foil using a short-haired brush. The electrode samples were dried at  $60^\circ\text{C}$  for 10 min and annealed at various temperatures ( $200\text{--}500^\circ\text{C}$ ) for 10 min in air. This brushing-annealing cycle was repeated to load different masses of  $MnO_x$  ( $1\text{--}10\text{ mg cm}^{-2}$ ). After the final cycle, the electrodes were additionally annealed for 1 h. Unless otherwise specified,  $MnO_x$  was annealed at  $400^\circ\text{C}$  with a loading mass of  $7\text{ mg cm}^{-2}$ .

The surface morphologies of the as-synthesized samples (particles and/or electrodes) were analyzed by scanning electron microscopy (SEM, Su-8230, Hitachi) at an accelerating voltage of 5.0 kV. A high-resolution field-emission transmission electron microscope (HR-FE-TEM, JEOL, JEM-2100 F) equipped with energy-dispersive spectroscopy (EDS, X-MaxN80, Horiba) was employed at an accelerating voltage of 200 kV. The surface areas of the powders were determined using the Brunauer–Emmett–Teller (BET; Micrometrics, ASAP 2020) method with  $N_2$  as the adsorbate gas. X-ray diffraction (XRD, PANalytical EMPUR-EAN) with Cu-K $\alpha$  radiation (40 kV and 30 mA) and X-ray photoelectron spectroscopy (XPS, Thermo Fisher Scientific) with Al-K $\alpha$  ( $h\nu = 1486.6\text{ eV}$ ) were performed to examine the crystalline patterns and elemental states of the as-synthesized samples, respectively.

### 2.2. Electrochemical activity tests and characterization

Linear sweep voltammograms of the as-synthesized electrodes (working electrodes) were obtained at a scan rate of  $5\text{ mV s}^{-1}$  with a saturated calomel electrode (SCE, reference electrode) and Pt wire (counter electrode) using an electrochemical workstation (Ivium) in aqueous saline solutions with various compositions at pH 6 (0.0137–0.941 M NaCl, 0.5 M NaCl with 5 mM NaClO, and 0.4 M NaCl with 100 mM NaClO) or artificial seawater (Instant Ocean, salinity  $36\text{ g L}^{-1}$ ) at pH 8.2. NaClO $_4$  (0.0137–0.5 M) was used instead of NaCl to examine the chloride effect where necessary. For bulk electrolysis, the as-synthesized PRT or  $MnO_x$  electrodes were held at constant  $J$  values



**Scheme 1.** Illustration of seawater electrolysis with a  $PtRuTiO_x$  (PRT) anode and  $MnO_x$  cathode pair in a membraneless single-compartment cell. Conventional seawater electrolysis proceeds under alkaline conditions ( $pH > 13$ ) to secure selectivity of OER over ClOR. In addition, it usually requires membranes to inhibit ClRR and HER, while separating  $H_2$  from  $O_2$ . However, if the electrolysis products are only HClO (and/or  $ClO^-$ ) in solution and  $H_2$  in headspace at Faradaic efficiencies of  $\sim 100\%$  for ClOR and HER, respectively, membranes for separating gases ( $H_2$  from  $O_2$ ) and inhibiting chlorine reduction at the cathode are not necessary.

(10–800 mA cm<sup>-2</sup>) in saline and seawater solutions in a single-compartment cell or two-compartment cell divided with a cation exchange membrane (CEM, CMI-7000S, Membranes International) (open or sealed to the atmosphere) while recording the electrode potentials ( $E$ ) with respect to the SCE. When the PRT and MnO<sub>x</sub> were coupled as the anode and cathode, respectively, a constant cell  $J$  ( $J_{\text{cell}}$ ) of 80 mA cm<sup>-2</sup> was applied, and the resulting cell voltage ( $E_{\text{cell}}$ ) was recorded using a direct current power supply (Agilent E3633A). During the bulk electrolysis, the solution was intermittently sampled and the free chlorines (represented by HClO/ClO<sup>-</sup>) were quantified using the *N,N*-diethyl-*p*-phenylenediamine reagent by the Hach method, as described elsewhere [15–17,34,35]. The evolved gases in the cell headspace were also analyzed for O<sub>2</sub> and H<sub>2</sub> using a gas chromatograph (GC, Agilent 7820 A; Inficon Micro GC Fusion) equipped with dual flame ionization and thermal conductivity detectors. For in situ, real-time analysis of O<sub>2</sub> and H<sub>2</sub> gases during prolonged bulk electrolysis over 100 h, the PRT anode/MnO<sub>x</sub> cathode pair at a distance of 30 mm was placed in an air-tight single-compartment cell through which N<sub>2</sub>-sparged seawater (pH 8.2) continuously flowed at a rate of 11 mL min<sup>-1</sup> using a peristaltic pump (BT100–2 J-19). During electrolysis, evolved gases with high-purity N<sub>2</sub> carrier gas (>99.99%) flowed through the headspace of the cell at a rate of 20 mL min<sup>-1</sup> and entered into a quadrupole mass spectrometer (Quality Mass Spectrometer, Hiden, GB/QIC-20). The composition of the headspace O<sub>2</sub> and H<sub>2</sub> gases was calibrated using standard gases. Simultaneously, free chlorine in the electrolyzed seawater was analyzed.

The electrochemical impedance spectroscopy of the as-synthesized PRT and MnO<sub>x</sub> electrodes was conducted at 1.1 and –1.5 V vs. SCE in the frequency ranges of 100 kHz to 0.1 Hz and 50 kHz to 0.01 Hz, respectively, with an amplitude of 10 mV. The double-layer capacitance

values of the electrodes proportional to the electrochemically active surface area were also examined by cyclic voltammetry in the  $E$  ranges of 0.85–0.95 V vs. SCE and –0.2 to –0.1 V vs. SCE, respectively, at varying scan rates in the range 20–100 mV s<sup>-1</sup>. The Faradaic efficiencies (FEs) for the ClOR, ClRR, HER, and OER were estimated using the following equation:

$$\text{FE (\%)} = [\Delta P_c \times n_c \times F \times 100\%] / (J \times t)$$

where  $\Delta P_c$ ,  $n_c$ ,  $F$ , and  $t$  refer to the amount (mol) of compounds produced (HClO, H<sub>2</sub>, and O<sub>2</sub>) or consumed (HClO), stoichiometric number of such compounds ( $n_c = 2$  for HClO and H<sub>2</sub>;  $n_c = 4$  for O<sub>2</sub>), Faraday constant (96,486 C mol<sup>-1</sup>), and time (s), respectively. Hereafter, SCE is omitted for working electrodes with half-reactions, unless otherwise mentioned.

### 3. Results and discussion

#### 3.1. Achieving high efficiency ClOR with durable PRT electrodes

The crystalline structures of the as-synthesized binary PR (Pt<sub>0.2</sub>Ru<sub>0.8</sub>O<sub>y</sub>) and ternary PRT (PRT-0.3) particles were examined (Fig. 1a). The PR sample (annealed at 500 °C) exhibited characteristic diffraction patterns of metallic Pt (PDF no. 04–0802 with  $2\theta = 39.76^\circ$ ,  $46.23^\circ$ ,  $67.45^\circ$ ,  $81.29^\circ$ , and  $85.71^\circ$  for (111), (200), (220), (311), and (222), respectively) and RuO<sub>2</sub> (PDF no. 40–1290 with  $2\theta = 28.01^\circ$ ,  $35.05^\circ$ ,  $40.02^\circ$ ,  $40.06^\circ$ , and  $54.25^\circ$  for (110), (101), (200), (111), and (211), respectively). Traces of metallic Ru peaks were also found at  $2\theta = 42.15^\circ$  (002) and  $44.01^\circ$  (101) (PDF no. 06–0663), which disappeared upon oxidative annealing at a higher temperature (Fig. S1). The PRT

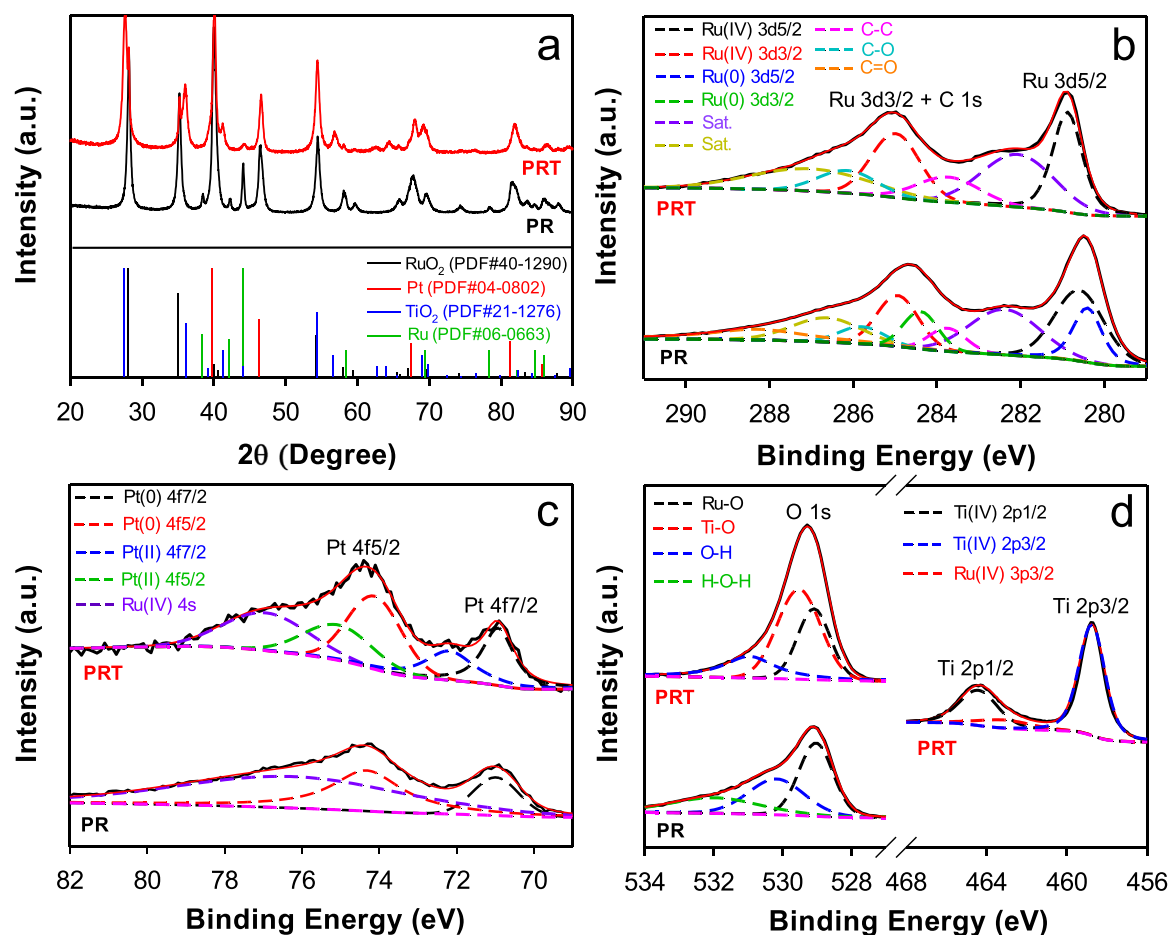


**Fig. 1.** Surface characterization of as-synthesized binary PR (Pt<sub>0.2</sub>Ru<sub>0.8</sub>O<sub>y</sub>) and ternary PRT (Pt<sub>0.06</sub>Ru<sub>0.24</sub>Ti<sub>0.7</sub>O<sub>y</sub>) particles annealed at 500 °C. (a) XRD spectra. (b-d) XPS spectra (b: Ru 3d, c: Pt 4f, and d: Ti 2p and O 1s). Deconvoluted XPS spectra are shown as dashed lines.



sample annealed at 500 °C displayed a mixture of RuO<sub>2</sub> and rutile TiO<sub>2</sub> (PDF no. 21-1276 with  $2\theta = 27.45^\circ, 36.09^\circ, 41.23^\circ, 54.32^\circ, 56.64^\circ$ , and  $69.01^\circ$  for (110), (101), (111), (211), (220), and (301), respectively), along with Pt diffraction peaks.

The XPS spectra further revealed the elemental states of the as-synthesized PR and PRT particles (Fig. 1b–d). For both samples, the Ru 3d spectra showed the spin-orbit doublet at binding energies of 280.9 eV (Ru 3d<sub>5/2</sub>) and 285 eV (Ru 3d<sub>3/2</sub>) (Fig. 1b). The Ru 3d<sub>3/2</sub> band appeared to be mixed with the C 1 s band, which was attributed to intrinsic or adsorbed carbon impurities. This was confirmed by the C 1 s band observed for the PR sample annealed at 800 °C (Fig. S2). Notably, the binding energy of the Ru 3d bands with the PRT sample was higher than that of the PR sample by 0.4 eV, owing to the dominant Ru<sup>4+</sup> species and absence of Ru<sup>0</sup> in the PRT sample. The Pt 4f bands in the PRT sample were located at 70.9 eV (Pt 4f<sub>7/2</sub>) and 74.6 eV (Pt 4f<sub>5/2</sub>), and the deconvolution of the bands revealed the coexistence of Pt<sup>0</sup> and Pt<sup>2+</sup> (Fig. 1c). In contrast, only Pt<sup>0</sup> was found in the PR sample, and Pt<sup>2+</sup> species were formed upon calcination at a high temperature (800 °C) (Fig. S2). The broad shoulder bands at ~76.4 eV were attributed to the Ru<sup>4+</sup> 4s band. This suggests that TiO<sub>2</sub> facilitated the oxidation of Ru<sup>3+</sup> and Pt<sup>0</sup> to Ru<sup>4+</sup> and Pt<sup>2+</sup>, respectively, during the oxidative annealing process at 500 °C. Moreover, the shifts in the Ru 3d and Pt 4f bands upon the introduction of TiO<sub>2</sub> indicate strong interactions between Ru and Pt with TiO<sub>2</sub>. The Ti 2p band of the PRT sample also shows the characteristic doublet spectra of 2p<sub>3/2</sub> (458.8 eV) and 2p<sub>1/2</sub> (464.3 eV), attributed to the Ti<sup>4+</sup> species (Fig. 1d). The contribution of the Ru 3p<sub>3/2</sub> band was observed in the deconvoluted Ti 2p band. Finally, the O 1s bands of the PR and PRT samples were compared. The deconvoluted three sub-bands in the PR sample were assigned to lattice oxygen (Ru-O-

Ru at 529.1 eV), surface oxygen (Ru-OH at 530.2 eV), and adsorbed oxygen (e.g., H<sub>2</sub>O at 532.1 eV) [39]. Although an additional lattice oxygen (Ti-O-Ti at 529.7 eV) was found in the PRT sample, the contribution of the adsorbed oxygen was negligible.

The as-synthesized PR sample was composed of irregularly shaped particles (Fig. 2a), and the primary particle size increased with the annealing temperature (Fig. S3). In contrast, the PRT sample displayed a relatively uniform spherical configuration with an average diameter of ~27 nm (Fig. 2b). The isotherm N<sub>2</sub> adsorption-desorption curves indicated a negligible interaction of N<sub>2</sub> with Pt, whereas N<sub>2</sub> adsorption was enhanced with Ru (and consequently PR) (Fig. 2c). Notably, the PRT sample exhibited a significantly high adsorption capacity with hysteresis (Fig. S4), indicating a mesoporous structure. The BET surface areas with Pt, Ru, and PR samples were < 10 m<sup>2</sup> g<sup>-1</sup>, whereas the PRT exhibited surface areas of > 40 m<sup>2</sup> g<sup>-1</sup> because of TiO<sub>2</sub> (Fig. 2c inset). The HR-TEM analysis of the PRT sample showed aggregates with primary particles of 10–20 nm (Fig. S5). Magnified HR-TEM images further revealed mixed interplanar spacings of 0.248 and 0.323 nm corresponding to the (101) and (110) planes of rutile TiO<sub>2</sub>, respectively, 0.316 nm corresponding to the (110) plane of RuO<sub>2</sub>, and 0.227 nm corresponding to the (111) plane of Pt (Fig. 2d). These crystalline planes were intimately connected to each other, forming strong interfacial contacts and an overlapping electronic structure [40,41]. Discrete Pt and RuO<sub>2</sub> particles were located on the TiO<sub>2</sub> surface, indicating that TiO<sub>2</sub> effectively inhibited the aggregation of the metal particles. The selected area electron diffraction (SAED) pattern further confirmed the coexistence of ternary crystalline structures with TiO<sub>2</sub>, RuO<sub>2</sub>, and Pt (Fig. 2e), which is in good agreement with the XRD and HR-TEM images. The EDS and elemental mapping analysis clearly showed a uniform distribution of Ru,

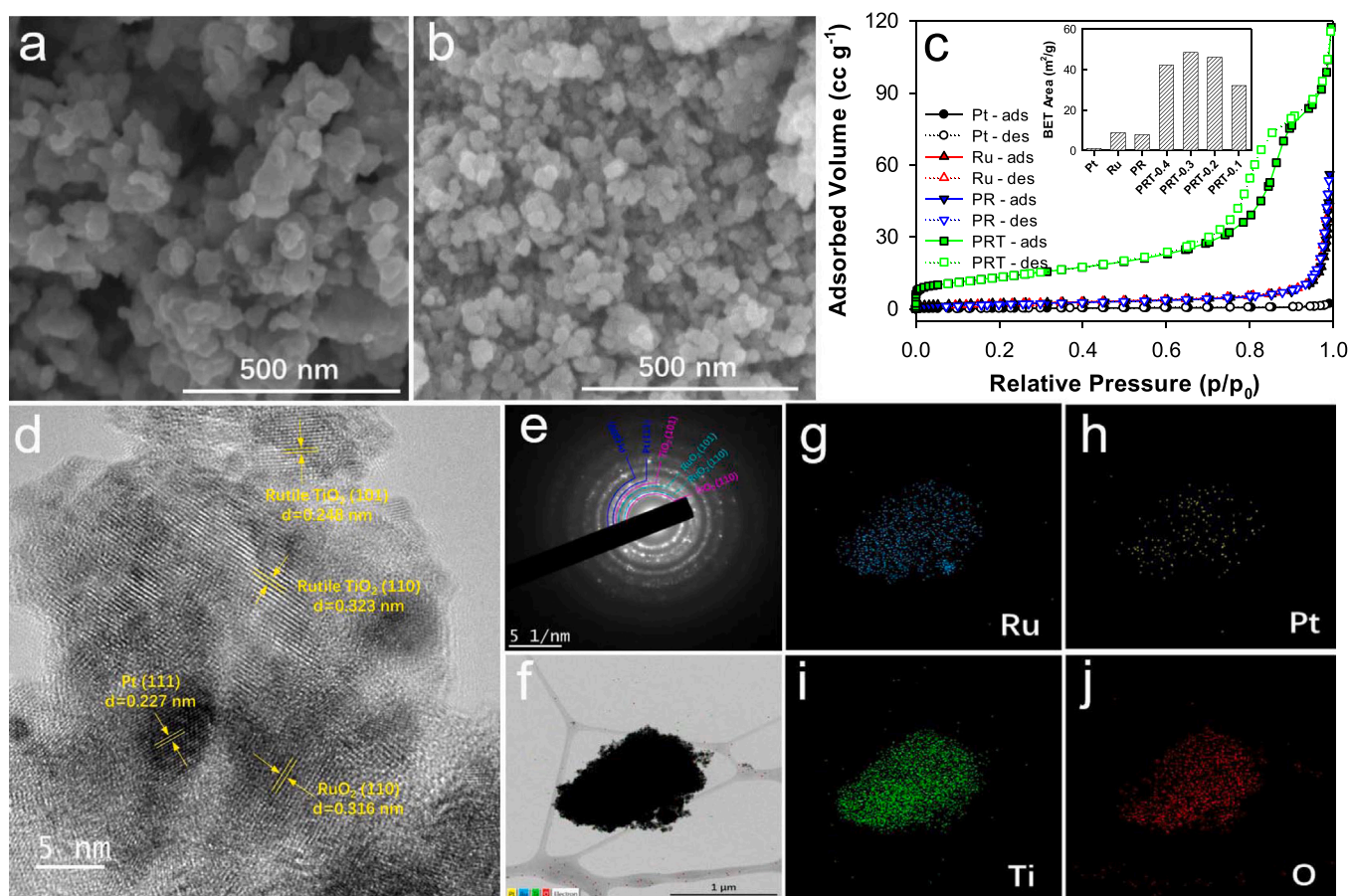


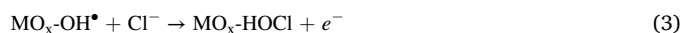
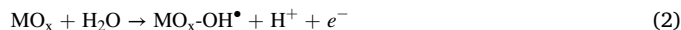
**Fig. 2.** (a and b) SEM images of as-synthesized PR and PRT particles, respectively. (c) Isotherm N<sub>2</sub> adsorption-desorption curves with the as-synthesized Pt, RuO<sub>2</sub>, PR, and PRT samples. Inset shows BET surface areas. (d and e) HR-TEM image and SAED pattern of the PRT sample. (f–j) EDS and elemental mappings of the PRT sample.

Pt, Ti, and O; however, the Pt signal was weak owing to the low Pt content (~6%) (Fig. 2f–j).

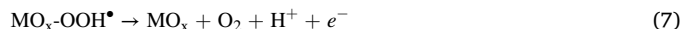
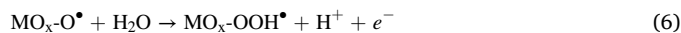
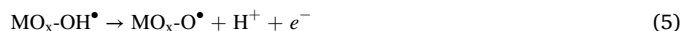
The as-synthesized binary PR and ternary PRT particles were sprayed onto Ti meshes, and the electrochemical behavior of the as-sprayed electrodes was examined in NaCl and NaClO<sub>4</sub> electrolytes. The linear sweep voltammograms with the PR electrode showed an onset potential ( $E_{on}$ ) value of ~0.95 V in both electrolytes, whereas a larger  $J$  was obtained in the NaCl electrolyte (Fig. 3a). A similar tendency was also observed with single Ru (i.e., RuO<sub>2</sub>) and Pt electrodes; however, the Pt electrode was nearly inactive in both solutions. The ternary PRT followed the same tendency, but the voltammogram difference between NaCl and NaClO<sub>4</sub> was significant. In the NaCl solution, the optimal PR fraction was found to be 0.3 (i.e., PRT-0.3 or Pt<sub>0.06</sub>Ru<sub>0.24</sub>Ti<sub>0.7</sub>O<sub>y</sub>), beyond which the electrochemical activity decreased (Fig. S6). Considering that OER is the primary oxidation reaction in a chloride-free solution (i.e., NaClO<sub>4</sub>) whereas a combination of ClOR and OER can occur in a chloride solution, an enhanced  $J$  value with NaCl may indicate that ClOR was favored over OER with PR and more significantly with PRT.

To quantitatively compare the ClOR efficiency, bulk electrolysis with various electrodes at  $J = 80 \text{ mA cm}^{-2}$  was performed (Fig. 3b). In 0.5 M NaCl, free chlorine (i.e., HClO/ClO<sup>−</sup>) was linearly produced with time (Fig. 3b inset), maintaining a ClOR-FE value of ~100% with the PRT electrode. This FE value was higher than that with the PR electrode (~84%), although the molar amounts of Pt and Ru in the PRT electrode were only 30% of those in the PR electrode. Moreover, each Pt and Ru exhibited considerably lower ClOR-FE values (<60%). As the electrolyte concentration decreased to 0.137 and 0.0137 M, respectively, the voltammogram difference with PRT between NaCl and NaClO<sub>4</sub> gradually reduced (Fig. S7). Nevertheless, ~100% ClOR-FE with PRT was obtained in 0.137 M NaCl. When the loading amount of PRT (3.33 mg cm<sup>−2</sup>) was reduced by 75% (0.83 mg cm<sup>−2</sup>; denoted as PRT (1/4)),  $E_{on}$  increased by +0.08 V and  $E$  increased to 0.5 V for  $J = 80 \text{ mA cm}^{-2}$ . This larger  $E$  value was attributed to the reduced active surface area of the catalysts. For example, the masses of the Pt and Ru salts with PRT (1/4) decreased to 0.073 and 0.135 mg cm<sup>−2</sup>, respectively. Nevertheless, ~100% ClOR-FE was achieved with PRT (1/4)

(Fig. 3b). Under the same electrolysis conditions, the OER with PRT was remarkably inhibited with an FE of < 1% (Fig. 3a inset). These results indicate that the as-synthesized PRT was highly selective for ClOR (reactions 2–4).



MO<sub>x</sub> represents the metal oxide surface. For the OER, the adsorbed OH<sup>•</sup> needs to be further oxidized to OOH<sup>•</sup> (reactions 5–7).



A comparison of the ClOR and OER mechanisms [33] indicates that PRT effectively catalyzed reaction 3 while inhibiting reaction 5.

The electrocatalytic activity of the as-synthesized electrodes is associated with the electrochemical active surface area (ECSA, defined as  $C_{dl} / C_s$ , where  $C_{dl}$  is the double layer capacitance and  $C_s$  is the specific capacitance). The  $C_{dl}$  value for PRT-0.3 was estimated to be ~5.7 mF cm<sup>−2</sup>, which was higher than the values for single and binary composition electrodes (0.05, 3.1, and 2.3 mF cm<sup>−2</sup> for Pt, Ru, and PR, respectively) and also the values for other ternary PRT electrodes (Figs. 3c and S8).  $C_{dl}$  appeared to be largely influenced by oxides (TiO<sub>2</sub> and RuO<sub>2</sub>), while  $C_s$  is usually considered constant at 40 μF cm<sup>−2</sup> [42]. The ECSA-normalized voltammograms further showed a significant decrease in the  $J$  values with PRT (Fig. S9). This indicates that the high activity of PRT was partially attributed to the enhanced ECSA. PRT-0.3 also exhibited the lowest interfacial charge-transfer resistance ( $R_{ct}$ ) (Fig. S10). Electrochemical impedance spectroscopic analysis revealed that PRT-3 had the smallest  $R_{ct}$  value (35.7 Ω) among the PRT series. The single and binary electrodes exhibited large  $R_{ct}$  values (Pt: 2700 Ω, Ru: 414 Ω, PR: 213 Ω). These results partly explain the superior activity

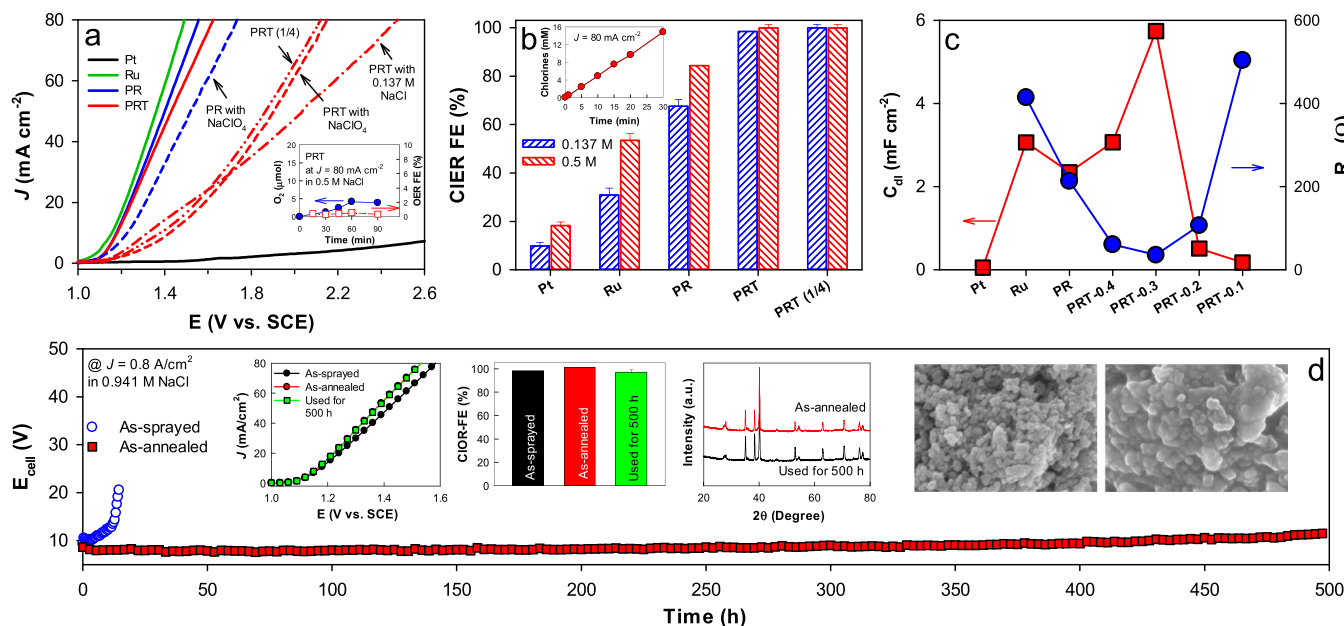


**Fig. 3.** (a) Linear sweep voltammograms with Pt, Ru, PR, and PRT electrodes in 0.5 M NaCl solutions at pH 6. For comparison, 0.137 M NaCl or 0.5 M NaClO<sub>4</sub> (pH 6) were also used. PRT (1/4) refers to the PRT with loading mass of 0.83 mg cm<sup>−2</sup>. The inset shows the O<sub>2</sub> evolution and its FE with PRT at  $J = 80 \text{ mA cm}^{-2}$  in 0.5 M NaCl. (b) FE values of ClOR at  $J = 80 \text{ mA cm}^{-2}$ . The inset shows the free chlorine production with time at  $J = 80 \text{ mA cm}^{-2}$  in 0.5 M NaCl. (c)  $C_{dl}$  and  $R_{ct}$  values. (d) Prolonged electrolysis with the as-sprayed and as-annealed PRT anodes at  $J = 800 \text{ mA cm}^{-2}$  in 0.941 M NaCl. Insets show voltammograms and FE values (at  $J = 80 \text{ mA cm}^{-2}$ ) of the as-sprayed, as-annealed, and 500 h-used PRT electrodes in 0.5 M NaCl solutions. XRD spectra and SEM images (left: as-annealed, right: used for 500 h) are also shown.

of PRT-0.3 compared to that of all other single, binary, and ternary compositions. It appeared that Pt and Ru were active components catalyzing CIOR, while  $\text{TiO}_2$  increased the surface area and promoted the active sites.

The stability of the optimized PRT electrode was examined under severe conditions ( $J = 800 \text{ mA cm}^{-2}$ ;  $0.941 \text{ M NaCl}$ ) while recording  $E_{\text{cell}}$  of the PRT anode and the mesh-type Ti cathode pair (Fig. 3d).  $E_{\text{cell}}$  was  $10.5 \text{ V}$  in the initial stage and abruptly increased to  $> 20 \text{ V}$  at  $\sim 10 \text{ h}$ . The PRT particles immobilized on the substrate (Ti mesh) via a spray process readily peeled off from the substrate after  $10 \text{ h}$ . Hence, the as-sprayed PRT electrode was annealed at  $300^\circ\text{C}$  for  $6 \text{ h}$  to induce robust contact, and its stability was tested again. The initial value of  $E_{\text{cell}}$  ( $8.5 \text{ V}$ ) was maintained over  $400 \text{ h}$ , and only slightly increased to  $\sim 11 \text{ V}$  after  $500 \text{ h}$ . The voltammograms of the annealed PRT electrodes (before and after  $500 \text{ h}$  of electrolysis) were the same, whereas their  $J$  values were larger than those of the as-sprayed PRT, which was attributed to the enhanced contact of the catalysts with the substrate upon annealing (Fig. 3d inset). The CIOR-FE value of the  $500 \text{ h}$ -used PRT electrode was  $\sim 97\%$ , which was nearly the same as that of the as-annealed electrode. In addition, the crystalline structure (XRD in Fig. 3d inset) and elemental states (XPS in Fig. S11) did not change after  $500 \text{ h}$  of electrolysis. However, the catalyst surface appeared to melt, and the particles became aggregated (SEM in Fig. 3d inset). This phenomenon of interparticle fusion is typical.[39,43,44] Nevertheless, the as-observed electrocatalytic activity and stability were outstanding compared to those obtained in previous reports (Table S1).

### 3.2. Inhibiting CIORR with $\text{MnO}_x$ electrodes

For suppression of the CIORR,  $\text{MnO}_x$  electrodes were synthesized at

various temperatures. The  $\text{MnO}_x$  electrode synthesized at  $200^\circ\text{C}$  ( $\text{MnO}_x$ -200) demonstrated an inhomogeneous cracked morphology, whereas compact uniform particles were observed in the  $\text{MnO}_x$ -400 sample (Fig. S12). The XRD spectra of both samples exhibited the same diffraction patterns corresponding to  $\text{Mn}_2\text{O}_3$  (PDF no. 24-0508;  $2\theta = 23.12^\circ, 32.92^\circ, 38.20^\circ, 45.14^\circ, 49.32^\circ, 55.14^\circ$ , and  $65.72^\circ$  for the (211), (222), (400), (323), (413), (044), and (622) planes, respectively) (Figs. 4a and S13). The HR-TEM images of the  $\text{MnO}_x$ -400 sample demonstrated an interplanar spacing of  $0.2714 \text{ nm}$ , corresponding to the (222) plane of  $\text{Mn}_2\text{O}_3$  (Fig. 4b). XPS analysis was performed to examine the Mn valence states of both samples (Fig. 4c). The Mn 2p bands ( $2p_{1/2}$  and  $2p_{3/2}$  at binding energies of  $653.4 \text{ eV}$  and  $641.6 \text{ eV}$ , respectively) in both samples appeared similar, and the deconvolution of the bands with  $\text{MnO}_x$ -400 revealed mixed Mn(II), Mn(III), and Mn(IV) sub-bands at fractions of  $30\%$ ,  $37\%$ , and  $33\%$ , respectively ( $31\%$ ,  $39\%$ , and  $30\%$  for  $\text{MnO}_x$ -200, respectively). The binding energy differences between the two Mn 3s bands were estimated to be  $5.2 \text{ eV}$  and  $5.3 \text{ eV}$ , respectively (Fig. 4d). This indicated that the average oxidation states of the surface Mn atoms were  $\sim 3.1$  and  $\sim 3.0$  for  $\text{MnO}_x$ -200 and  $\text{MnO}_x$ -400, respectively [45,46]. The as-synthesized  $\text{MnO}_x$  electrodes exhibited various  $C_{\text{dl}}$  and  $R_{\text{ct}}$  values depending on the annealing temperature (Fig. 4e). Among the samples,  $\text{MnO}_x$ -400 showed the highest  $C_{\text{dl}}$  value ( $6.97 \text{ mF cm}^{-2}$ ) and the lowest  $R_{\text{ct}}$  value ( $209 \Omega$ ) (Fig. S14 and S15).  $\text{MnO}_x$ -200 demonstrated the second highest  $C_{\text{dl}}$  ( $3.89 \text{ mF cm}^{-2}$ ) but the worst  $R_{\text{ct}}$ . The  $C_{\text{dl}}$  of  $\text{MnO}_x$ -500 was as small as that of the Ti substrate, but the  $R_{\text{ct}}$  value was comparable to that of  $\text{MnO}_x$ -400. The electrocatalytic activities of the as-synthesized  $\text{MnO}_x$  electrodes (deposited on a Ti plate) were examined for the CIORR and HER in NaCl solutions (with and without NaClO). The voltammograms of  $\text{MnO}_x$ -400 indicated an  $E_{\text{on}}$  of approximately  $-1.8 \text{ V}$  (corresponding to  $-1.2 \text{ V}$  vs. reversible

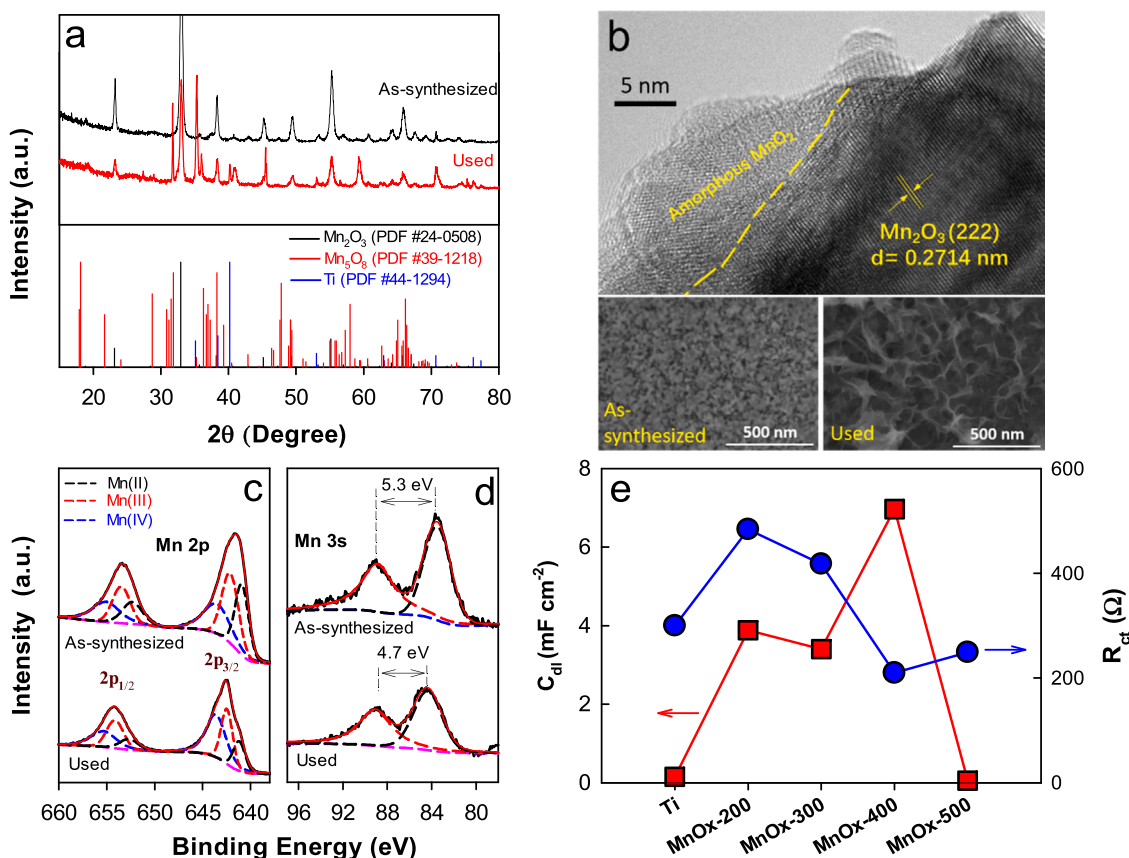
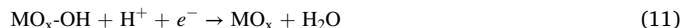


**Fig. 4.** Surface and electrochemical analysis of  $\text{MnO}_x$  electrodes (deposited on Ti plates) annealed at various temperatures ( $200$ – $500^\circ\text{C}$ ). Unless otherwise specified,  $\text{MnO}_x$  stands for  $\text{MnO}_x$ -400 (annealed at  $400^\circ\text{C}$ ). (a) XRD spectra, (b) HR-TEM and SEM images (top and bottom panels, respectively), (c and d) XPS spectra (Mn 2p and Mn 3s, respectively), and (e)  $C_{\text{dl}}$  and  $R_{\text{ct}}$ . After  $100 \text{ h}$  of electrolysis, the used  $\text{MnO}_x$  samples were also examined with XRD, SEM, and XPS.



hydrogen electrode (RHE)), regardless of the presence of NaClO (Fig. 5a). This indicates a negligible CIRR with HClO/CIO<sup>-</sup>. In contrast, the Ti plate (without MnO<sub>x</sub> catalysts) exhibited an  $E_{on}$  of approximately -1.7 V (corresponding to -1.1 V vs. RHE) in a 0.5 M NaCl solution. The voltammogram gradually shifted to a positive potential in the presence of 5 mM and 100 mM NaClO, with  $E_{on}$  values of -1.6 and -1.4 V, respectively. Notably, two distinct reduction peaks were observed at -0.55 V and -1.04 V with 100 mM NaClO due to the CIRR [38,47]. For comparison, voltammograms with Pt electrodes were also examined.  $E_{on}$  with a Pt electrode exhibited a more positive value than the corresponding values with Ti and MnO<sub>x</sub> in the NaCl solution. In addition, the voltammogram shifted to a positive potential in the presence of NaClO, and CIRR peaks were observed. These behaviors indicate that Pt should also be active in the CIRR. Bulk electrolysis for the CIRR was further performed using 5 mM NaClO (Fig. 5b). For the Pt and Ti substrates at  $J = -10 \text{ mA cm}^{-2}$ , the concentrations of chlorine ( $C_t / C_0$ ) linearly decreased with time with a CIRR-FE of 18–20%. This decrease in chlorine concentration was significantly inhibited by the MnO<sub>x</sub> electrodes. Among them, MnO<sub>x</sub>-400 required the smallest  $E$  value at  $J = -10 \text{ mA cm}^{-2}$  (Fig. S16), with a CIRR-FE of approximately 3% (Fig. 5b inset). The CIRR typically proceeds with HClO/CIO<sup>-</sup> adsorption, followed by breaking of the Cl–O bond, and regeneration of the oxidized surface with concurrent H<sub>2</sub>O release (reactions 8–11, where MO<sub>x</sub> represents the metal oxide surface) [48].



Considering that the isoelectric point of MnO<sub>x</sub> was located at pH < ~4 (Fig. S17) [49], the HClO/CIO<sup>-</sup> access (reaction 8) should be inhibited to the negatively charged MnO<sub>x</sub> surface at a circumneutral pH value [25].

The CIRR-FE was significantly influenced by the type of electrode, NaClO concentration, and  $J$  value (Fig. 5c). For the Ti substrate with 5 mM NaClO, the CIRR-FE value gradually decreased with increasing  $J$  because of the concurrent HER. With 100 mM NaClO, the CIRR-FEs with the Ti were ~100% at  $J \leq -30 \text{ mA cm}^{-2}$  and decreased to ~65% at larger  $J$  values. A similar behavior was observed for Pt, albeit with lower CIRR-FE values than those for Ti at  $J \geq -30 \text{ mA cm}^{-2}$  with 100 mM NaClO. This indicates that the HER occurred more efficiently with Pt than with Ti, particularly at high concentrations of NaClO. In contrast, the CIRR-FEs with MnO<sub>x</sub> were < 3% at all the tested  $J$  values with 5 mM NaClO. With 100 mM NaClO, a volcanic CIRR-FE profile was obtained by blocking the HClO access at a low  $J$  and by a competitive HER at a high  $J$ . MnO<sub>x</sub>, Ti, and Pt electrodes produced H<sub>2</sub> in NaCl solutions with 5 mM NaClO at  $J = -10 \text{ mA cm}^{-2}$ , leading to HER-FEs of > 90%, ~65%, and ~55%, respectively (Fig. 5d). When the NaClO concentration increased to 100 mM, no H<sub>2</sub> was evolved with Ti and Pt (hence, zero HER-FEs). However, nearly the same amounts of H<sub>2</sub> were produced with MnO<sub>x</sub> with 5 mM and 100 mM NaClO (hence, similar HER-FEs). These results confirm that MnO<sub>x</sub> is highly selective for the HER in saline water containing chlorines.

The stability of the as-synthesized MnO<sub>x</sub> electrode was further tested over 100 h at  $J = -10 \text{ mA cm}^{-2}$  and  $-80 \text{ mA cm}^{-2}$  in 0.5 M NaCl solutions.  $E$  values of approximately -3.5 V and -4.2 V, respectively,

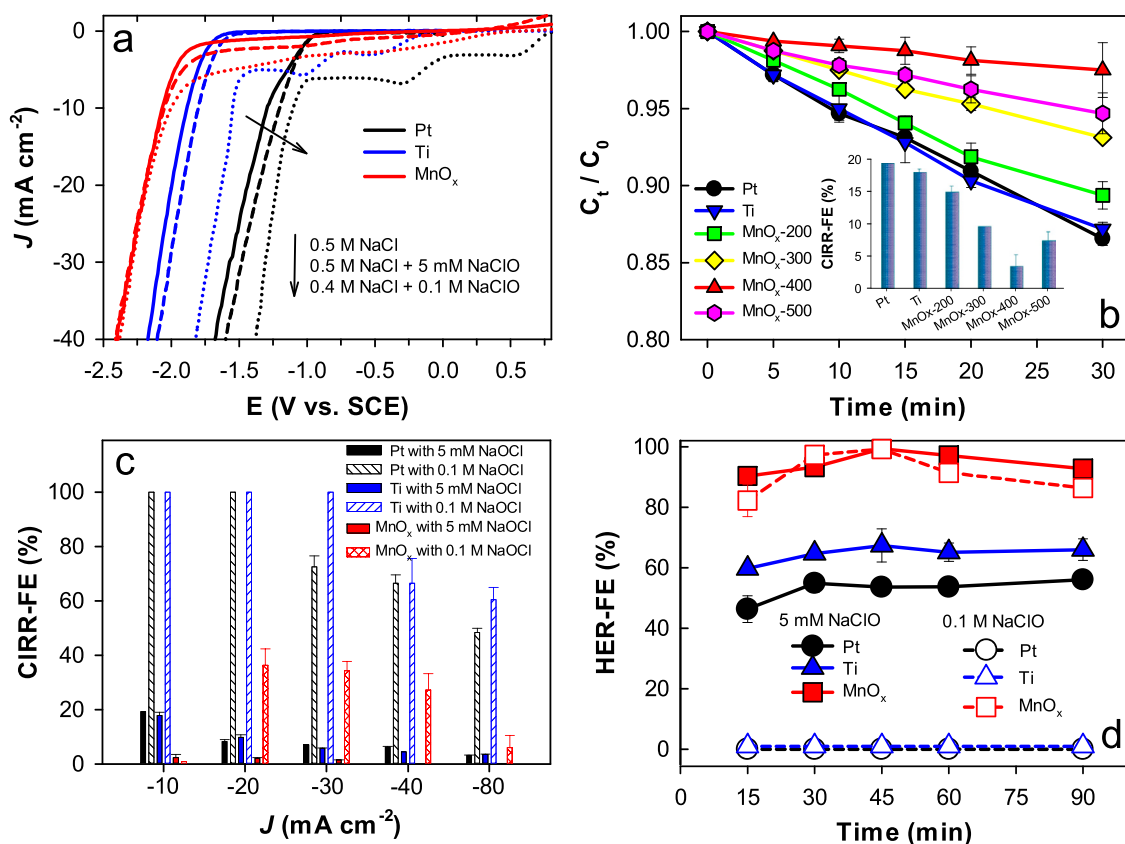


**Fig. 5.** Electrochemical behavior and activities for CIRR and HER with Pt, Ti, and MnO<sub>x</sub> electrodes in 0.5 M NaCl, 0.5 M NaCl with 5 mM NaClO, or 0.4 M NaCl with 0.1 M NaClO solutions at pH 6. Unless otherwise specified, MnO<sub>x</sub> stands for MnO<sub>x</sub>-400 (annealed at 400 °C). (a) Linear sweep voltammograms. (b) Changes in the concentration of chlorines ( $C_t / C_0$ ) with various electrodes at  $J = -10 \text{ mA cm}^{-2}$  in 0.5 M NaCl with 5 mM NaClO in a two-compartment cell divided by a CEM. The inset shows CIRR-FE values in 30 min (c) CIRR-FE values as a function of  $J$  and NaOCl concentration. (d) HER-FE changes at  $J = -10 \text{ mA cm}^{-2}$  in 0.5 M NaCl with 5 mM NaClO.

were maintained over 100 h (Fig. S18). The used  $\text{MnO}_x$  electrode with  $J = -10 \text{ mA cm}^{-2}$  for 100 h exhibited new crystalline structures originating from  $\text{Mn}_5\text{O}_8$  (Fig. 4a). The particle-compact surface also changed into an unfolded tissue-like surface (Fig. 4b). A deconvolution of the Mn 2p bands further revealed a fractional ratio of 17/32/51 for Mn(II)/Mn(III)/Mn(IV) (Fig. 4c), whereas the average oxidation state of the Mn atom increased from 3.0 to  $\sim 3.7$  (Fig. 4d). Despite the cathodic reaction, this increase in the oxidation state can be attributed to the hypochlorite-mediated partial oxidation of  $\text{MnO}_x$  [25].

### 3.3. Membraneless seawater electrolysis and production of pure $\text{H}_2$ gas

The as-synthesized PRT and  $\text{MnO}_x$  electrodes were wired in a membraneless single-compartment cell containing seawater at a pH of 8.2. The  $E_{\text{on}}$  values in the anodic and cathodic voltammograms were slightly different from those in 0.5 M NaCl at pH 6 (Fig. 6a), likely owing to different pH values and composition [50]. The voltammograms further indicated that an anode/cathode cell potential ( $E_{\text{cell}}$ ) of  $\sim 4.8 \text{ V}$  ( $= 1.8 \text{ V} - (-3 \text{ V})$ ) was required for  $J_{\text{cell}} = 80 \text{ mA cm}^{-2}$ . Under galvanostatic conditions at  $J_{\text{cell}} = 80 \text{ mA cm}^{-2}$ , chlorine was linearly produced with a ClOR-FE of  $\sim 100\%$  (Fig. 6b). This FE value was the same as that obtained for the two-compartment cell equipped with a membrane (Fig. 3). When  $\text{MnO}_x$  was replaced with a Ti plate, the ClER-FE gradually decreased to  $\sim 80\%$  owing to the concurrent ClRR with the Ti plate. This ClRR should compete with the HER, thereby lowering the HER-FE to  $\sim 80\%$  (Fig. 6c). In contrast, an HER-FE of  $\sim 100\%$  was obtained with the PRT/ $\text{MnO}_x$  pair.

Prolonged electrolysis of seawater was conducted in a continuous-flow, membraneless reactor equipped with a PRT/ $\text{MnO}_x$  pair (Fig. 6d). The headspace gases were monitored in situ in real time using a quadrupole mass spectrometer. At  $J_{\text{cell}} = 80 \text{ mA cm}^{-2}$ , an  $E_{\text{cell}}$  of  $\sim 4.8 \text{ V}$  was stably maintained over 100 h, whereas ClOR occurred at an FE of  $\sim 100\%$ , and the OER-FE was  $< 0.5\%$  (virtually zero).  $\text{H}_2$  gas was

continuously produced with an FE of approximately 100%. No changes in the  $E_{\text{cell}}$  and FE values were observed during electrolysis. These results clearly indicate that the PRT/ $\text{MnO}_x$  pair is effective in producing high-purity  $\text{H}_2$  gas via membraneless seawater electrolysis.

## 4. Conclusions

This study successfully demonstrated the production of high-purity  $\text{H}_2$  using a ClOR-selective anode and HER-selective cathode pair via membraneless electrolysis of undisturbed, unbuffered seawater. An optimized ternary PRT electrocatalyst with a minimized Pt level exhibited superior activity compared with single and binary component catalysts for the selective production of chlorines in saline and seawater, with complete inhibition of the OER. Such an activity can be attributed to the excellent surface and electrochemical characteristics of the PRT electrocatalyst, including a large surface area and low interfacial charge-transfer resistance. The PRT electrocatalyst maintained industry-level stability with constant ClOR activity over 500 h under severe conditions. Moreover,  $\text{MnO}_x$  drove the HER at an FE of  $\sim 100\%$  in the presence of free chlorines while completely inhibiting the ClRR. In contrast, the ClRR and HER occurred concurrently with other commonly used electrodes (Ti and Pt), reducing the HER efficiency. The observed selectivity of the HER with  $\text{MnO}_x$  was associated with the limited interaction of free chlorines. Finally, the PRT anode/ $\text{MnO}_x$  cathode pair produced  $\text{H}_2$  gas at an FE of  $\sim 100\%$  via seawater electrolysis at pH 8.2 over 100 h in a membraneless reactor. No  $\text{O}_2$  was evolved, whereas ClOR occurred at an FE of  $\sim 100\%$  during seawater electrolysis. The as-developed electrolyzer does not require the use of membranes for producing high-purity  $\text{H}_2$  with an FE of  $\sim 100\%$  via unbuffered natural seawater electrolysis.

### CRediT authorship contribution statement

Nan-Nan Liang: Methodology, Validation, Formal analysis,

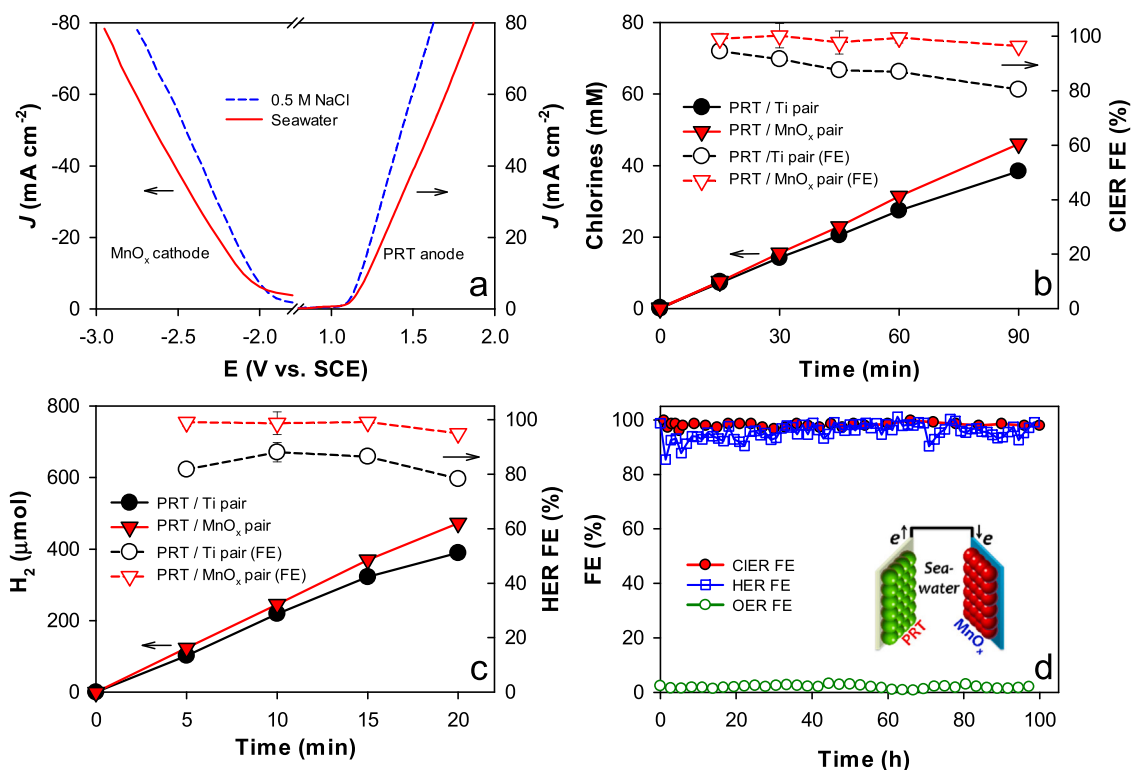


**Fig. 6.** Seawater electrolysis with a PRT anode and  $\text{MnO}_x$  cathode (PRT/ $\text{MnO}_x$ ) pair in a single-compartment cell. (a) Linear sweep voltammograms of each electrode in 0.5 M NaCl and seawater solution (salinity  $36 \text{ g L}^{-1}$ ). (b) Production of chlorines and ClOR-FEs with PRT/Ti and PRT/ $\text{MnO}_x$  pairs at  $J_{\text{cell}} = 80 \text{ mA cm}^{-2}$  in seawater solution. (c) Production of  $\text{H}_2$  and HER-FEs with PRT/Ti and PRT/ $\text{MnO}_x$  pairs at  $J_{\text{cell}} = 80 \text{ mA cm}^{-2}$  in seawater solution. (d) Prolonged electrolysis with the PRT/ $\text{MnO}_x$  pair at  $J_{\text{cell}} = 80 \text{ mA cm}^{-2}$  in seawater solution. Evolved  $\text{H}_2$  and  $\text{O}_2$  gases were in situ real time measured while chlorines were intermittently analyzed.



Investigation. **Dong Suk Han:** Formal analysis, Writing – review & editing. **Hyunwoong Park:** Conceptualization, Methodology, Validation, Formal analysis, Resources, Writing – original draft, Writing – review & editing, Visualization, Supervision, Project administration, Funding acquisition.

## Declaration of Competing Interest

The authors declare that they have no known competing financial interests or personal relationships that could have appeared to influence the work reported in this paper.

## Data availability

Data will be made available on request.

## Acknowledgments

This research was supported by the National Research Foundation of Korea (2018R1A6A1A03024962, 2019R1A2C2002602, and 2021K1A4A7A02102598). This publication was made possible by a grant from the Qatar National Research Fund under its National Priorities Research Program (NPRP 13S-0202-200228).

## Appendix A. Supplementary material

Supplementary data associated with this article can be found in the online version at [doi:10.1016/j.apcatb.2022.122275](https://doi.org/10.1016/j.apcatb.2022.122275).

## References

- [1] G. Kakoulaki, I. Kougias, N. Taylor, F. Dolci, J. Moya, A. Jäger-Waldau, Green hydrogen in Europe – a regional assessment: substituting existing production with electrolysis powered by renewables, *Energy Convers. Manag.* 228 (2021), <https://doi.org/10.1016/j.enconman.2020.113649>.
- [2] M. Yue, H. Lambert, E. Pahon, R. Roche, S. Jemei, D. Hissel, Hydrogen energy systems: a critical review of technologies, applications, trends and challenges, *Renew. Sustain. Energy Rev.* 146 (2021), <https://doi.org/10.1016/j.rser.2021.111180>.
- [3] J. Ivy, Summary of Electrolytic Hydrogen Production: Milestone Completion Report, National Renewable Energy Laboratory (NREL/MP-560-36734), 2004.
- [4] M.A. Khan, T. Al-Attas, S. Roy, M.M. Rahman, N. Ghaffour, V. Thangadurai, S. Larter, J. Hu, P.M. Ajayan, M.G. Kibria, Seawater electrolysis for hydrogen production: a solution looking for a problem, *Energy Environ. Sci.* 14 (2021) 4831–4839, <https://doi.org/10.1039/d1ee00870f>.
- [5] M.R. Shaner, H.A. Atwater, N.S. Lewis, E.W. McFarland, A comparative technoeconomic analysis of renewable hydrogen production using solar energy, *Energy Environ. Sci.* 9 (2016) 2354–2371, <https://doi.org/10.1039/c5ee02573g>.
- [6] H. Park, Solar remediation of wastewater and saline water with concurrent production of value-added chemicals, *J. Environ. Chem. Eng.* 10 (2022), 106919, <https://doi.org/10.1016/j.jece.2021.106919>.
- [7] J. Kim, W.J.K. Choi, J. Choi, M.R. Hoffmann, H. Park, Electrolysis of urea and urine for solar hydrogen, *Catal. Today* 199 (2013) 2–7, <https://doi.org/10.1016/j.cattod.2012.02.009>.
- [8] H. Park, C.D. Vecitis, M.R. Hoffmann, Solar-powered electrochemical oxidation of organic compounds coupled with the cathodic production of molecular hydrogen, *J. Phys. Chem. A* 112 (2008) 7616–7626, <https://doi.org/10.1021/jp802807e>.
- [9] H. Park, C.D. Vecitis, W. Choi, O. Weres, M.R. Hoffmann, Solar-powered production of molecular hydrogen from water, *J. Phys. Chem. C* 112 (2008) 885–889, <https://doi.org/10.1021/jp710723p>.
- [10] H. Dagdougui, A. Ouammi, R. Sacile, A regional decision support system for onsite renewable hydrogen production from solar and wind energy sources, *Int. J. Hydrog. Energy* 36 (2011) 14324–14334, <https://doi.org/10.1016/j.ijhydene.2011.08.050>.
- [11] A. Christensen, Assessment of Hydrogen Production Costs from Electrolysis: United States and Europe, The International Council on Clean Transportation, 2020.
- [12] I.A. Gondal, Offshore renewable energy resources and their potential in a green hydrogen supply chain through power-to-gas, *Sustain. Energy Fuels* 3 (2019) 1468–1489, <https://doi.org/10.1039/c8se00544c>.
- [13] R. d'Amore-Domenech, T.J. Leo, Sustainable hydrogen production from offshore marine renewable farms: techno-energetic insight on seawater electrolysis technologies, *ACS Sustain. Chem. Eng.* 7 (2019) 8006–8022, <https://doi.org/10.1021/acssuschemeng.8b06779>.
- [14] S. Bolar, S. Shit, N. Chandra Murmu, T. Kuila, Progress in theoretical and experimental investigation on seawater electrolysis: opportunities and challenges, *Sustain. Energy Fuels* 5 (2021) 5915–5945, <https://doi.org/10.1039/d1se01347e>.
- [15] S. Kim, D.S. Han, H. Park, Reduced titania nanorods and Ni-Mo-S catalysts for photoelectrocatalytic water treatment and hydrogen production coupled with desalination, *Appl. Catal. B Environ.* 284 (2021), 119745, <https://doi.org/10.1016/j.apcatb.2020.119745>.
- [16] B.-j. Kim, G. Piao, S. Kim, S.Y. Yang, Y. Park, D.S. Han, H.K. Shon, M.R. Hoffmann, H. Park, High efficiency solar desalination accompanying electrocatalytic conversions of desalted chloride and captured carbon dioxide, *ACS Sustain. Chem. Eng.* 7 (2019) 15320–15328, <https://doi.org/10.1021/acssuschemeng.9b02640>.
- [17] S. Kim, G. Piao, D.S. Han, H.K. Shon, H. Park, Solar desalination coupled with water remediation and molecular hydrogen production: a novel solar water-energy nexus, *Energy Environ. Sci.* 11 (2018) 344–353, <https://doi.org/10.1039/C7EE02640D>.
- [18] H. Park, A. Bak, Y.Y. Ahn, J. Choi, M.R. Hoffmann, Photoelectrochemical performance of multi-layered BiO<sub>x</sub>-TiO<sub>2</sub>/Ti electrodes for degradation of phenol and production of molecular hydrogen in water, *J. Hazard. Mater.* 211 (2012) 47–54, <https://doi.org/10.1016/j.jhazmat.2011.05.009>.
- [19] H. Park, C.D. Vecitis, M.R. Hoffmann, Electrochemical water splitting coupled with organic compound oxidation: the role of active chlorine species, *J. Phys. Chem. C* 113 (2009) 7935–7945, <https://doi.org/10.1021/jp810331w>.
- [20] S. Khatun, H. Hirani, P. Roy, Seawater electrocatalysis: activity and selectivity, *J. Mater. Chem. A* 9 (2021) 74–86, <https://doi.org/10.1039/d0ta08709b>.
- [21] K.S. Exner, J. Anton, T. Jacob, H. Over, Controlling selectivity in the chlorine evolution reaction over RuO<sub>2</sub>-based catalysts, *Angew. Chem. Int. Ed.* 126 (2014) 11212–11215, <https://doi.org/10.1002/ange.201406112>.
- [22] S. Kim, S.K. Choi, B.Y. Yoon, S.K. Lim, H. Park, Effects of electrolyte on the electrocatalytic activities of RuO<sub>2</sub>/Ti and Sb-SnO<sub>2</sub>/Ti anodes for water treatment, *Appl. Catal. B Environ.* 97 (2010) 135–141, <https://doi.org/10.1016/j.apcatb.2010.03.033>.
- [23] Y.Y. Ahn, S.Y. Yang, C. Choi, W. Choi, S. Kim, H. Park, Electrocatalytic activities of Sb-SnO<sub>2</sub> and Bi-TiO<sub>2</sub> anodes for water treatment: effects of electrocatalyst composition and electrolyte, *Catal. Today* 282 (2017) 57–64, <https://doi.org/10.1016/j.cattod.2016.03.011>.
- [24] W. Choi, D.S. Han, H. Park, Reactive halogen species-mediated electrocatalytic oxidation of arsenite(III), *J. Phys. Chem. A* 126 (2022) 8459–8467, <https://doi.org/10.1021/acs.jpca.2c06479>.
- [25] B. Endrödi, A. Stojanovic, M. Cuartero, N. Simic, M. Wildlock, R. de Marco, G. A. Crespo, A. Cornell, Selective hydrogen evolution on manganese oxide coated electrodes: new cathodes for sodium chlorate production, *ACS Sustain. Chem. Eng.* 7 (2019) 12170–12178, <https://doi.org/10.1021/acssuschemeng.9b01279>.
- [26] S. Dresch, F. Dionigi, M. Klingenhof, P. Strasser, Direct electrolytic splitting of seawater: opportunities and challenges, *ACS Energy Lett.* 4 (2019) 933–942, <https://doi.org/10.1021/acsenenergylett.9b00220>.
- [27] L. Wu, L. Yu, B. McElhenny, X. Xing, D. Luo, F. Zhang, J. Bao, S. Chen, Z. Ren, Rational design of core-shell-structured CoP@FeOOH for efficient seawater electrolysis, *Appl. Catal. B* 294 (2021), <https://doi.org/10.1016/j.apcatb.2021.120256>.
- [28] F. Dionigi, T. Reier, Z. Pawolek, M. Glicch, P. Strasser, Design criteria, operating conditions, and nickel-iron hydroxide catalyst materials for selective seawater electrolysis, *ChemSusChem* 9 (2016) 962–972, <https://doi.org/10.1002/cssc.201501581>.
- [29] S. Jiang, H. Sun, H. Wang, B.P. Ladewig, Z. Yao, A comprehensive review on the synthesis and applications of ion exchange membranes, *Chemosphere* 282 (2021), 130817, <https://doi.org/10.1016/j.chemosphere.2021.130817>.
- [30] Y.S. Park, F. Liu, D. Diercks, D. Braaten, B. Liu, C. Duan, High-performance anion exchange membrane water electrolyzer enabled by highly active oxygen evolution reaction electrocatalysts: synergistic effect of doping and heterostructure, *Appl. Catal. B* 318 (2022) 12824, <https://doi.org/10.1016/j.apcatb.2022.121824>.
- [31] J.N. Hausmann, R. Schlögl, P.W. Menezes, M. Driess, Is direct seawater splitting economically meaningful, *Energy Environ. Sci.* 14 (2021) 3679–3685, <https://doi.org/10.1039/d0ee03659e>.
- [32] T.U. Hag, M. Pasha, Y. Tong, S.A. Mansour, Y. Haik, Au nanocluster coupling with Gd-Co<sub>2</sub>B nanoflakes embedded in reduced TiO<sub>2</sub> nanosheets: seawater electrolysis at low cell voltage with high selectivity and corrosion resistance, *Appl. Catal. B* 301 (2022), 120836, <https://doi.org/10.1016/j.apcatb.2021.120836>.
- [33] M. Panizza, G. Cerisola, Direct and mediated anodic oxidation of organic pollutants, *Chem. Rev.* 109 (2009) 6541–6569, <https://doi.org/10.1021/cr9001319>.
- [34] W. Choi, J.H. Choi, H. Park, Electrocatalytic activity of metal-doped SnO<sub>2</sub> for the decomposition of aqueous contaminants: Ta-SnO<sub>2</sub> vs. Sb-SnO<sub>2</sub>, *Chem. Eng. J.* 409 (2021), 128175, <https://doi.org/10.1016/j.cej.2020.128175>.
- [35] M. Wang, B.-j. Kim, D.S. Han, H. Park, Electrocatalytic activity of nanoparticulate TiO<sub>2</sub> coated onto Ta-doped IrO<sub>2</sub>/Ti substrates: effects of the TiO<sub>2</sub> overlayer thickness, *Chem. Eng. J.* 425 (2021), 131435, <https://doi.org/10.1016/j.cej.2021.131435>.
- [36] T. Lim, G.Y. Jung, J.H. Kim, S.O. Park, J. Park, Y.-T. Kim, S.J. Kang, H.Y. Jeong, S. K. Kwak, S.H. Joo, Atomically dispersed Pt-N<sub>4</sub> sites as efficient and selective electrocatalysts for the chlorine evolution reaction, *Nat. Commun.* 11 (2020) 412, <https://doi.org/10.1038/s41467-019-14272-1>.
- [37] B. Endrödi, V. Smulders, N. Simic, M. Wildlock, G. Mul, B. Mei, A. Cornell, In situ formed vanadium-oxide cathode coatings for selective hydrogen production, *Appl. Catal. B* 244 (2019) 233–239, <https://doi.org/10.1016/j.apcatb.2018.11.038>.
- [38] B. Endrödi, O. Diaz-Morales, U. Mattinen, M. Cuartero, A.K. Padinjarethil, N. Simic, M. Wildlock, G.A. Crespo, A. Cornell, Selective electrochemical hydrogen evolution on cerium oxide protected catalyst surfaces, *Electrochim. Acta* 341 (2020), <https://doi.org/10.1016/j.electacta.2020.136022>.
- [39] S. Panigrahy, R. Samanta, P. Panda, R. Mishra, S. Barman, RuO<sub>2</sub> as promoter in Pt-RuO<sub>2</sub> nanostructures/carbon composite, a pH universal catalyst for hydrogen

- evolution/oxidation reactions, *Int. J. Energy Res.* 46 (2021) 6406–6420, <https://doi.org/10.1002/er.7577>.
- [40] P. Zhu, X. Xiong, D. Wang, Regulations of active moiety in single atom catalysts for electrochemical hydrogen evolution reaction, *Nano Res.* 15 (2022) 5792–5815, <https://doi.org/10.1007/s12274-022-4265-y>.
- [41] R. Li, D. Wang, Understanding the structure-performance relationship of active sites at atomic scale, *Nano Res.* 15 (2022) 6888–6923, <https://doi.org/10.1007/s12274-022-4371-x>.
- [42] S. Jung, C.C.L. McCrory, I.M. Ferrer, J. Peters, T.F. Jaramillo, Benchmarking nanoparticulate metal oxide electrocatalysts for the alkaline water oxidation reaction, *J. Mater. Chem. A* 4 (2016) 3068–3076, <https://doi.org/10.1039/C5TA07586F>.
- [43] D. Wang, H.L. Xin, R. Hovden, H. Wang, Y. Yu, D.A. Muller, F.J. DiSalvo, H. D. Abruna, Structurally ordered intermetallic platinum-cobalt core-shell nanoparticles with enhanced activity and stability as oxygen reduction electrocatalysts, *Nat. Mater.* 12 (2013) 81–87, <https://doi.org/10.1038/nmat3458>.
- [44] J.C. Meier, I. Katsounaros, C. Galeano, H.J. Bongard, A.A. Topalov, A. Kostka, A. Karschin, F. Schüth, K.J.J. Mayrhofer, Stability investigations of electrocatalysts on the nanoscale, *Energy Environ. Sci.* 5 (2012), <https://doi.org/10.1039/c2ee22550f>.
- [45] E.S. Ilton, J.E. Post, P.J. Heaney, F.T. Ling, S.N. Kerisit, XPS determination of Mn oxidation states in Mn (hydr)oxides, *Appl. Surf. Sci.* 366 (2016) 475–485, <https://doi.org/10.1016/j.apsusc.2015.12.159>.
- [46] J. Guo, X. Zhang, X. Du, F. Zhang, A. Mn<sub>3</sub>O<sub>4</sub>, nano-wall array based binder-free cathode for high performance lithium–sulfur batteries, *J. Mater. Chem. A* 5 (2017) 6447–6454, <https://doi.org/10.1039/c7ta00475c>.
- [47] T. Watanabe, K. Akai, Y. Einaga, The reduction behavior of free chlorine at boron-doped diamond electrodes, *Electrochem. Commun.* 70 (2016) 18–22, <https://doi.org/10.1016/j.elecom.2016.06.010>.
- [48] K. Hedenstedt, A.S.O. Gomes, M. Busch, E. Ahlberg, Study of hypochlorite reduction related to the sodium chlorate process, *Electrocatalysis* 7 (2016) 326–335, <https://doi.org/10.1007/s12678-016-0310-5>.
- [49] H. Zhang, A. Wu, H. Fu, L. Zhang, H. Liu, S. Zheng, H. Wan, Z. Xu, Efficient removal of Pb(II) ions using manganese oxides: the role of crystal structure, *RSC Adv.* 7 (2017) 41228, <https://doi.org/10.1039/C7RA05955H>.
- [50] L. Yu, L. Wu, B. McElhenny, S. Song, D. Luo, F. Zhang, Y. Yu, S. Chen, Z. Ren, Ultrafast room-temperature synthesis of porous S-doped Ni/Fe (oxy)hydroxide electrodes for oxygen evolution catalysis in seawater splitting, *Energy Environ. Sci.* 13 (2020) 3439–3446, <https://doi.org/10.1039/d0ee00921k>.